Supporting Information

Defective phase engineering of S-Scheme TiO_2-SnS/SnS_2 core-shell Photocatalytic nanofibers for elevated Visible light responsive H_2 generation and Nitrogen fixation

Kugalur Shanmugam Ranjith[a], Seyed Majid Ghoreishian[b], Ali Mohammadi[a], Ganji Seeta Rama Raju[a], Yun Suk Huh[c,], Young-Kyu Han[a,*]*

[a]Department of Energy and Material Engineering, Dongguk University-Seoul, Seoul 04620, South Korea

[b]Department of Chemical Engineering, University of South Carolina, Columbia, SC, USA

[c]Department of Biological Engineering, Inha University, Incheon 22212, South Korea

[*]Corresponding authors: yunsuk.huh@inha.ac.kr (Y. S. Huh), ykenergy@dongguk.edu (Y.-K. Han)

1. Experimental details

1.1. Characterization details

The electrospun nanostructures were analyzed for morphology and the elemental content using a field emission scanning electron microscope (FESEM, Hitachi S-4700), an energy dispersive X-ray spectrometer (EDX)-equipped with high-resolution transmission electron microscopy (HRTEM, JEOL JEM-2100) at an accelerating voltage of 200 kV. Energy-dispersive X-ray spectroscopy (EDX) was utilized to confirm the composition and elemental mapping. The tructural features of the TiO_2-SnS heterostructures were measured by a PANalytical X'Pert multipurpose X-ray diffractometer with Cu Kα radiation. Using a JASCO V-770 UV–vis spectrophotometer and a FEX, NOST, Republic of Korea PL spectrophotometer, the UV–vis diffuse reflectance spectra (DRS) and photoluminescence (PL) measurements were obtained. The surface chemical composition was examined using Thermo K-alpha-monochromated X-ray photoelectron spectroscopy (XPS) with an Al K (1486.6 eV) source. After the samples were degassed for three hours at 200 °C, the Brunauer-Emmet-Teller (BET) analysis was used to determine the samples' specific surface area utilizing ASAP ZOZO (Micromeritics Co. USA). Using a UV-vis spectrophotometer (JASCO V-770), the UV-vis absorbance spectra of the pollutants were used to examine the dye degradation. A Bruker model A300 spectrometer (microwave frequency of 9.86 GHz, modulation amplitude of 3 G, modulation frequency of 100 kHz, microwave power of 6.37 mW, temperature of 298 K) was used to conduct electron paramagnetic resonance (EPR). Using HORIBA Delta Pro, time-resolved PL (TRPL) spectra were obtained at an excitation wavelength of 350 nm.

1.2. Photocatalytic experiments for H_2 evolution

The heterostructure catalyst (100 mg) with the TEOA aqueous solution (10%, 100 mL) serving as a trapping agent was sonicated for 10 min, and the mixture was introduced into a sealed glass reactor to investigate the photocatalytic hydrogen production from water splitting. The reactor was completely degassed to remove the air and stirred for 30 min in N_2 bubbling to maintain the atmosphere inert. A 300 W Xe lamp (PhotoFluorII) equipped with a UV-cut-off filter ($\lambda \geq 420$ nm) was used as the light source. The photo reactor had a quartz window with a top irradiation area of about 28.26 cm^2. During the reaction, the temperature was kept at 15 °C using cooling water circulation. The evolved H_2 was quantified by gas chromatography (GC) with a thermal conductive detector (TCD, connected to a TDX-01 molecular sieve column). Besides, N_2 was used as carrier gas. The apparent quantum yield (AQY) was calculated for different incident monochromatic wavelengths (365, 420, 450, 520, and 650 nm) according to the following equation:

$$AQE = \frac{2\ x\ numer\ of\ H_2\ molecules\ (n)}{Number\ of\ incident\ photos\ (N)} \qquad \text{.....(1)}$$

1.3. Photocatalytic experiments for N_2 fixation

The photocatalytic N_2 fixation reaction was performed under a 300 W Xe lamp (PhotoFluorII) equipped with a top-irradiated quartz reactor. Typically, 10 mg of photocatalyst was dispersed in 50 mL of distilled H_2O without any sacrificial agents and ultrasonicated for 10 min. The mixture was transferred into the reactor and vacuum-degassed for 30 min. Afterward, high-purity N_2 (>99.999%) bubbled into the system. The degassing and bubbling processes were repeated five times. Finally, the N_2 was bubbled for another 30 min before the light was turned on, and it

continued to bubble throughout the reaction process at a flow rate of 100 mL/min. The reactor was built with a water-circulating system to keep the temperature of the reaction environment constant at 2 °C. Under photoirradiation, every 30 min, 1 mL of liquid was collected and filtered with a 0.22 μm filter, and ammonia concentration was detected by Nessler's reagent method using UV spectrophotometry. Ar gas was purged at the same rate in the evacuated reaction vessel instead of N_2 for the control experimental condition. **Fig. S5** shows the calibration curve of Nessler's reagent method, with an R_2 value greater than 0.997.

1.4. Photoelectrochemical measurements

The measurement for the photocurrent, Mott-Schottky (M-S), linear sweep voltammetry, and electrochemical impedance (EIS) characterization were analyzed using Metrohm Autolab (PGSTAT302N) electrochemical workstation in a standard three-electrode system with Pt wire as counter electrode and Ag/AgCl (sat. KCl) as reference electrode. The catalytic slurry was loaded on a FTO substrate and used as a working electrode. The catalytic slurry was prepared by mixing catalyst (10 mg) and Nafion solution (5 wt%, 20 μL) in EtOH (0.5 mL). A 300 W Xe lamp (PhotoFluorII) equipped with a UV-cut-off filter ($\lambda \geq 420$ nm) was used as the light source. In this experiment, 0.5 M Na_2SO_4 aqueous solution was used as the electrolyte for the photo-responsive measurements.

1.5. Computational Methodology

After drawing the structures based on the XRD spectrum, the composite structure was optimized for declination the residual forces on the atoms to less than 0.03 $eV \cdot Å^{-1}$. Basic calculations with QuantumATK software. For bulk calculations, we employed the linear combination of atomic orbitals (LCAO) approach within the generalized gradient approximation (GGA) using the Perdew-Burke-Ernzerhof (PBE) functional. The basis set used was double zeta polarization (DZP) to ensure an accurate description of the electronic states. A density mesh cutoff of 80 Hartree was applied to improve the resolution of the charge density, and a grid spacing of 4.0 Å was used. Non-equilibrium Green's function (NEGF) Device Calculations: For the device simulations, we employed the NEGF formalism using the same LCAO-GGA method with the DZP basis set to describe the electronic structure. A Monkhorst-Pack k-point grid of 7×3×9 was chosen for accurate sampling along the device and transport directions. The density mesh cutoff was set to 80 Hartree to ensure convergence in charge and potential.

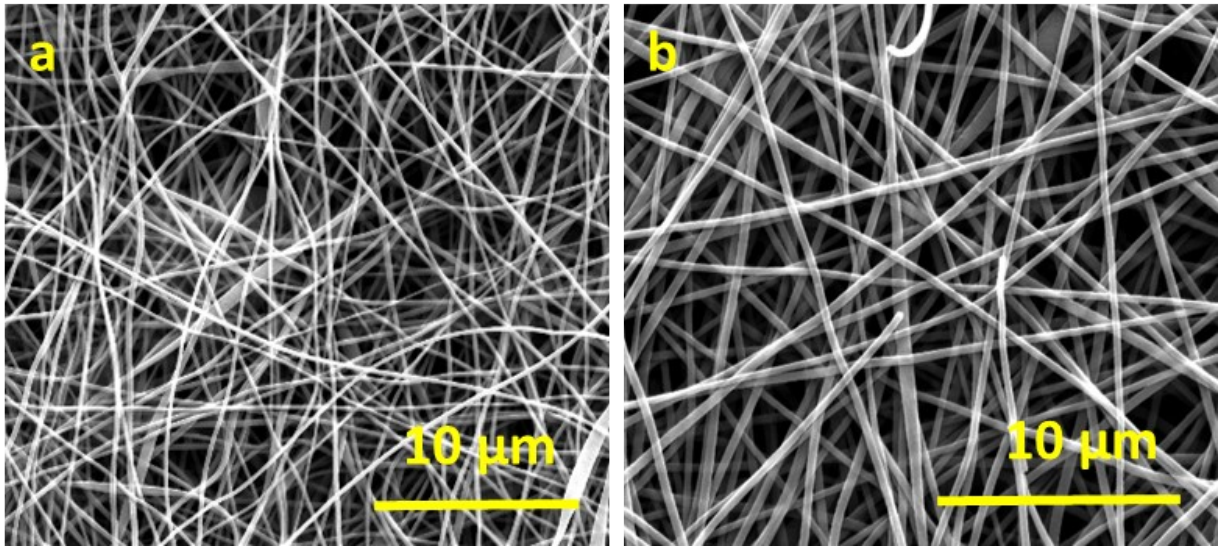

Fig. S1. FESEM images of The Ti-PVP and Ti/Sn-PVP based as prepared nanofibers. (a) Ti-PVP NFs, (b) Ti/Sn (0.4/0.2 mL h^{-1})-PVP core-shell NFs.

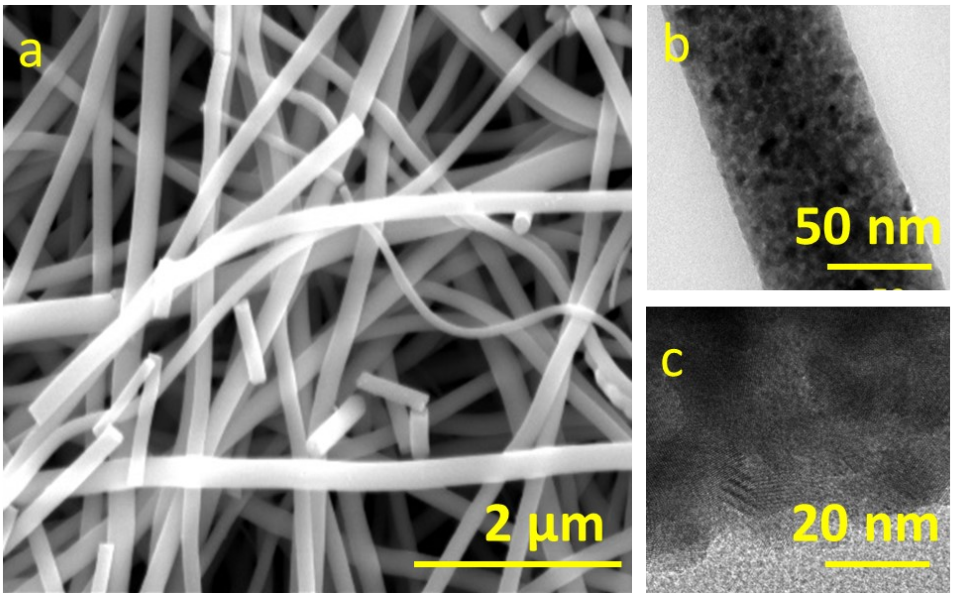

Fig. S2. SEM and TEM images of the TiO_2 nanofibers prepared through the electrospinning process.

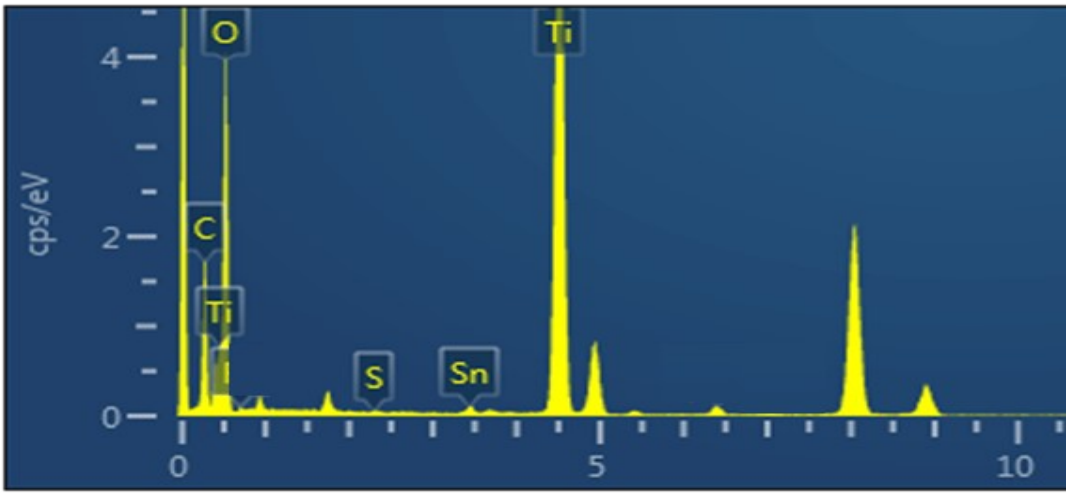

Fig. S3. EDAX spectra of the TiO_2-SnS/SnS_2 (2:2) NFs.

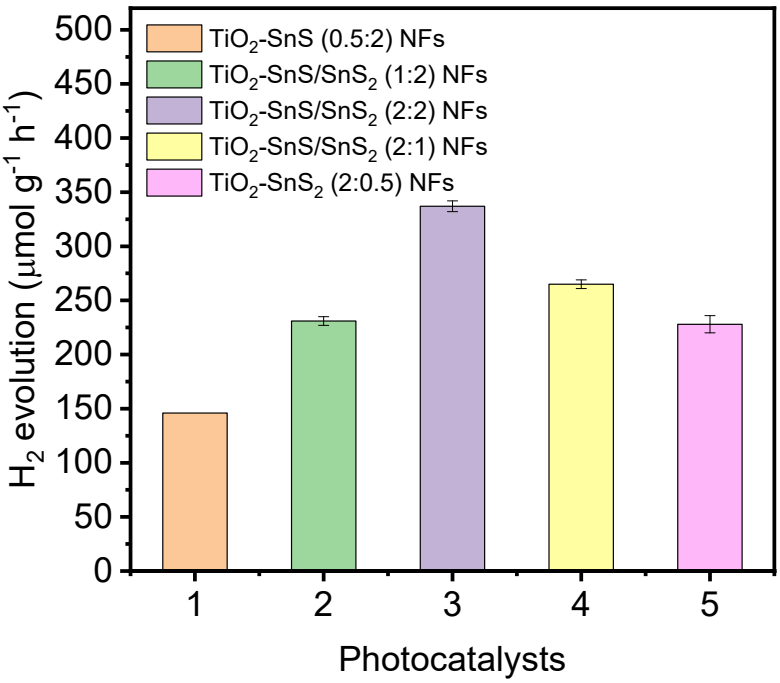

Fig. S4. Average rate of Photocatalytic H_2 evolution over TiO_2-based heterostructure NFs under visible irradiation.

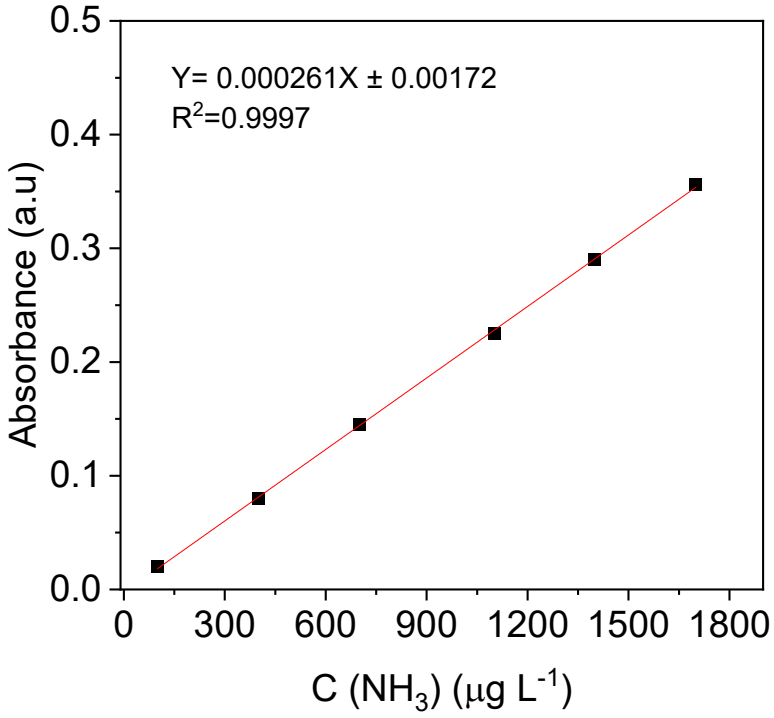

Fig. S5. The Standard curve of ammonia solution with different concentrations calculated from UV-Vis absorption spectra at λ=420 nm was measured using the Nessler reagent chromogenic method.

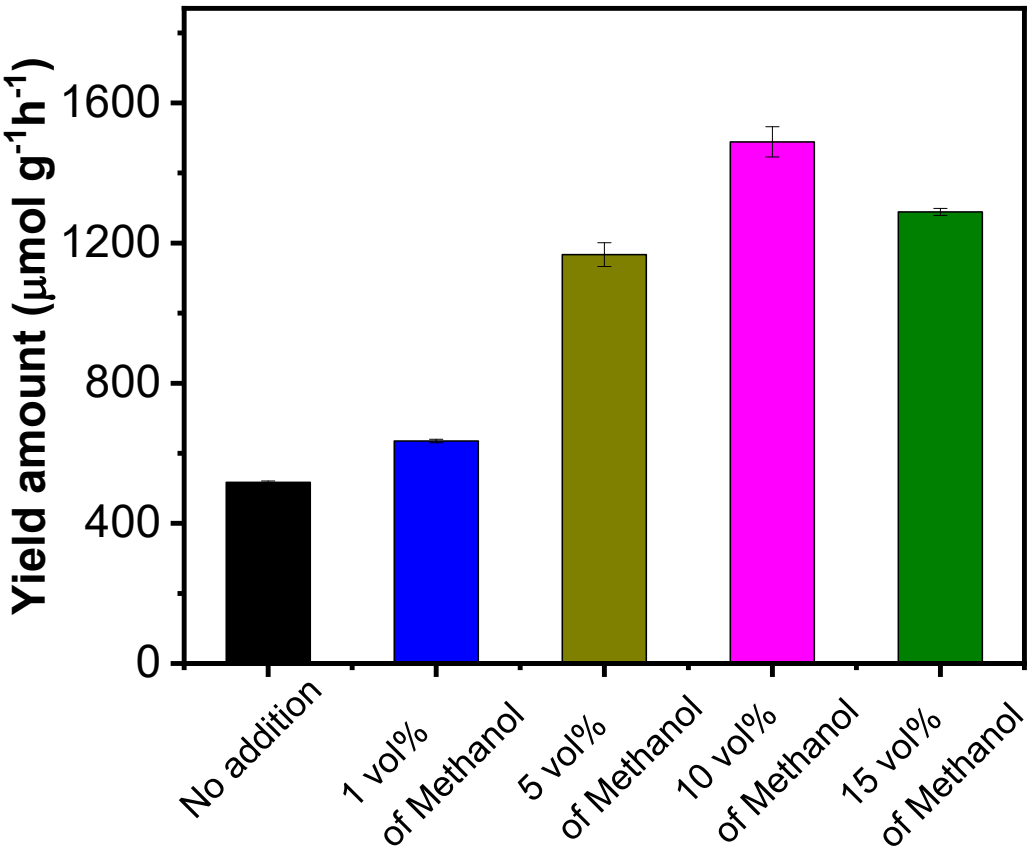

Fig. S6. NH_3 production rate over TiO_2-SnS/SnS_2 (2:2) NFs under visible irradiation (>420 nm) with adding different volume content of methanol.

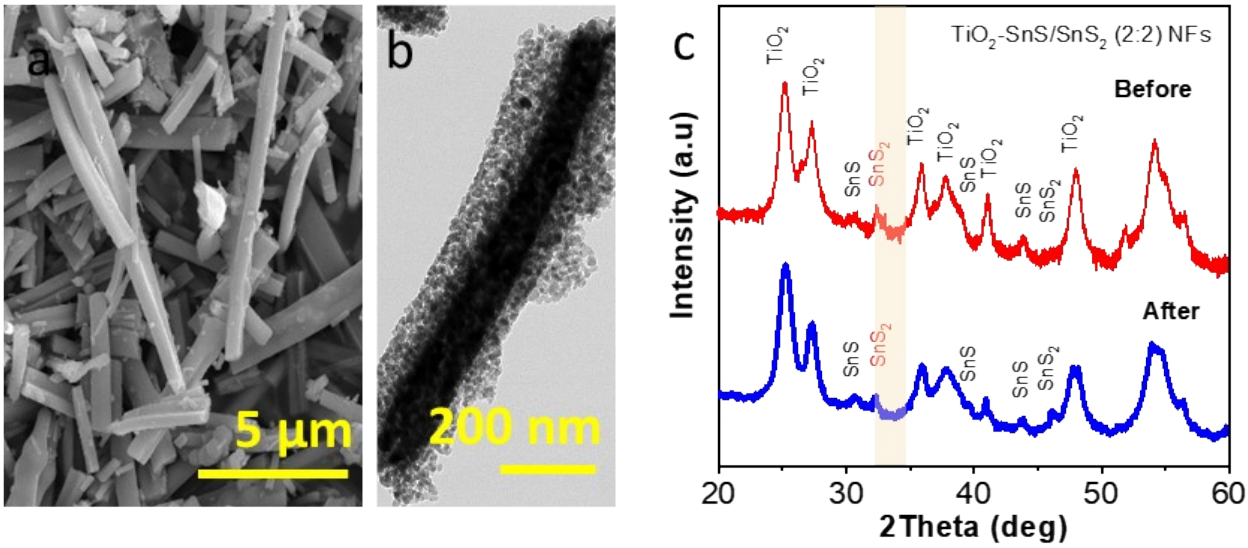

Fig. S7. (a, b) FE-SEM and TEM of the reused catalyst; (c) XRD of TiO_2-SnS/SnS_2 (2:2) NFs before and after the cyclic test.

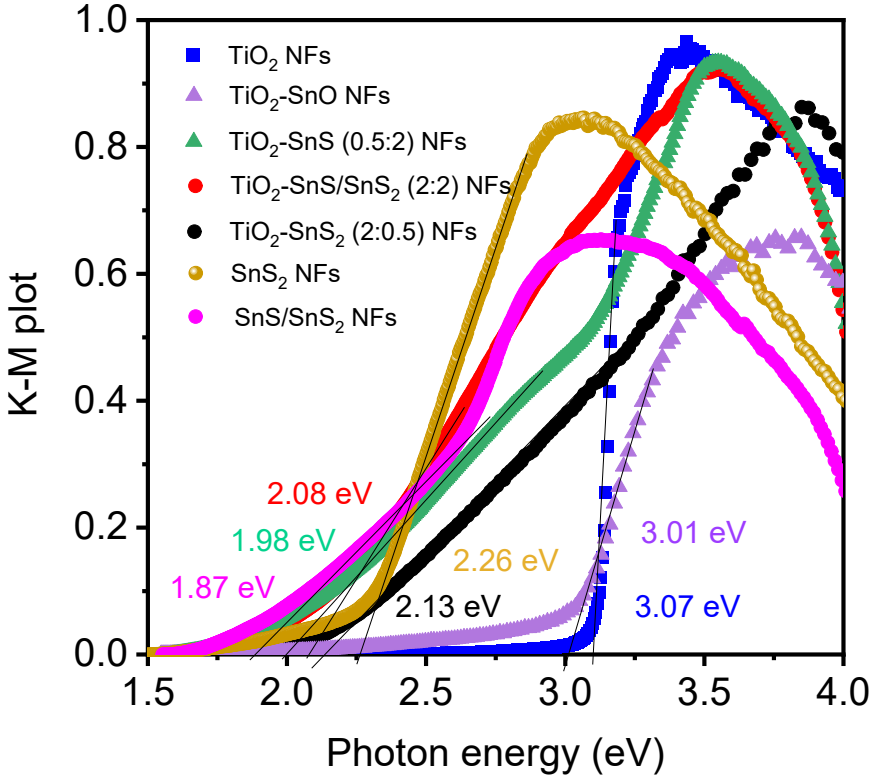

Fig. S8. (a) K-M plot for the TiO_2, SnS_2, SnS/SnS_2, and TiO_2 based heterostructure NFs.

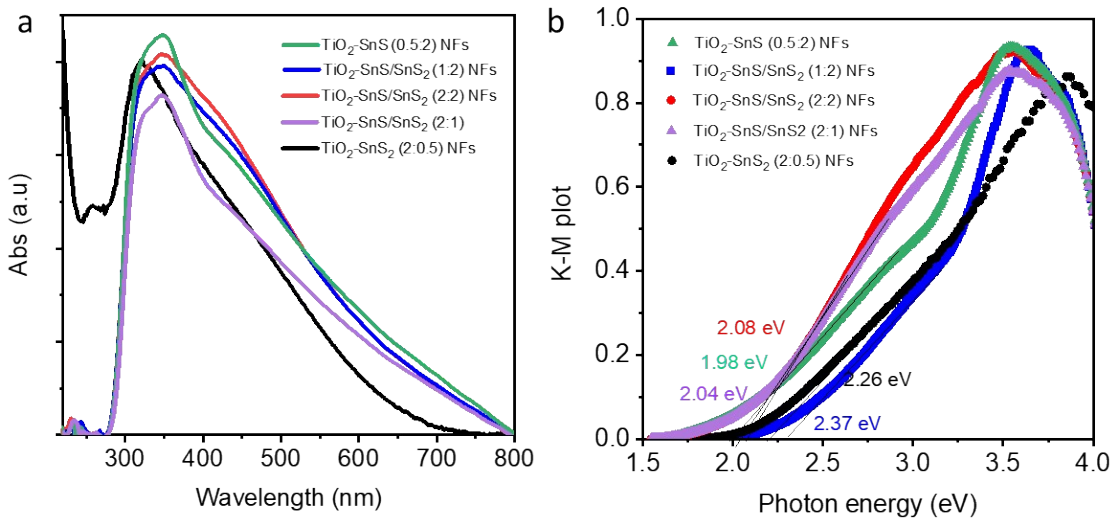

Fig. S9. (a) UV-Vis DRS, (b) K-M plot of TiO_2-SnS_x NFs.

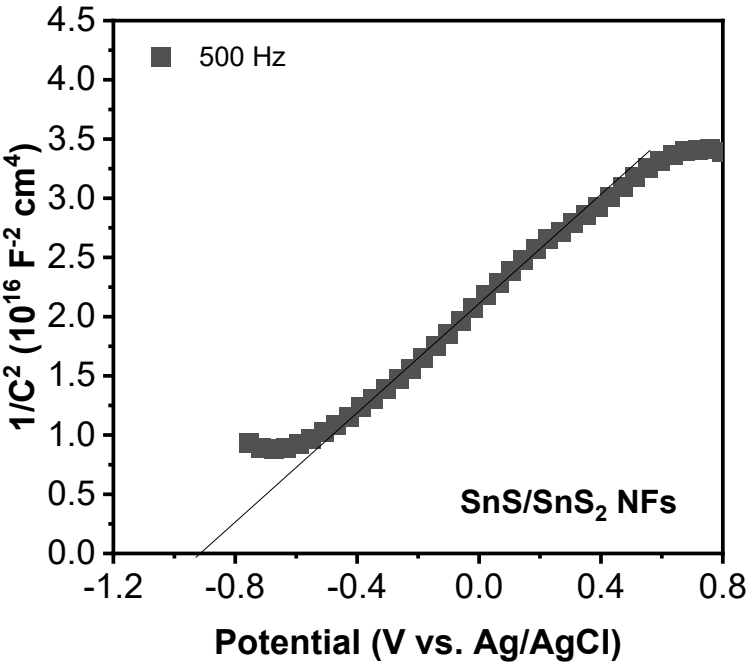

Fig. S10. Mott-Schottky plot of SnS/SnS_2 NFs.

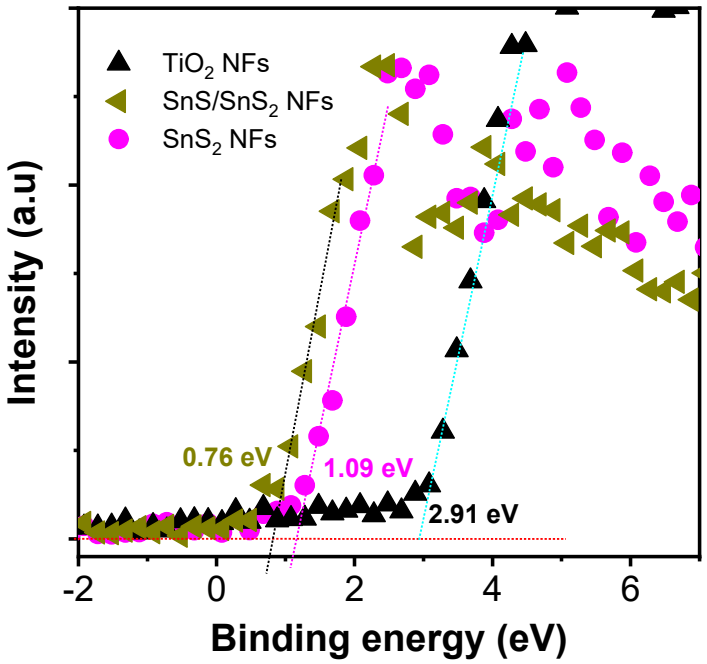

Fig. S11. XPS valence band spectra of SnS_2 and SnS/SnS_2 NFs.

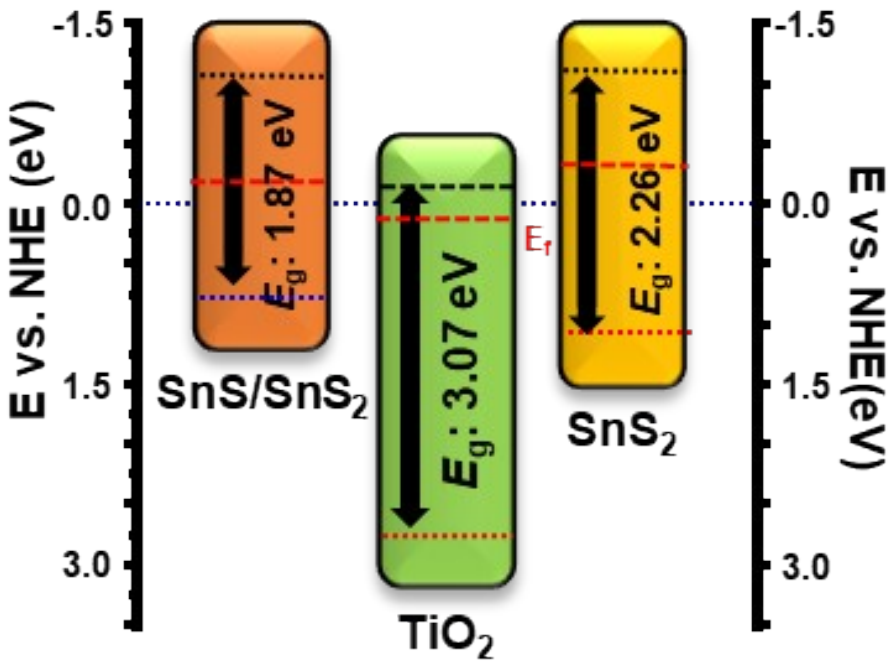

Fig. S12. Energy band structure TiO_2, SnS_2, SnS/SnS_2 before getting the heterostructure interface.

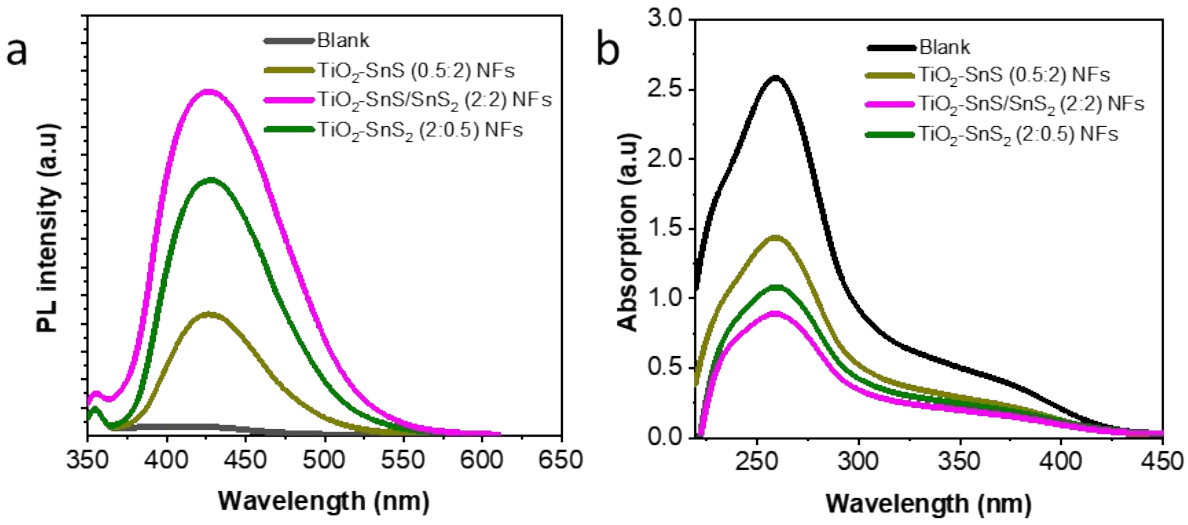

Fig. S13. (a) Fluorescence profile of terephthalic acid, and (b) NBT abs decrease rate in presence of TiO_2-SnS_x NFs under photo irradiation.

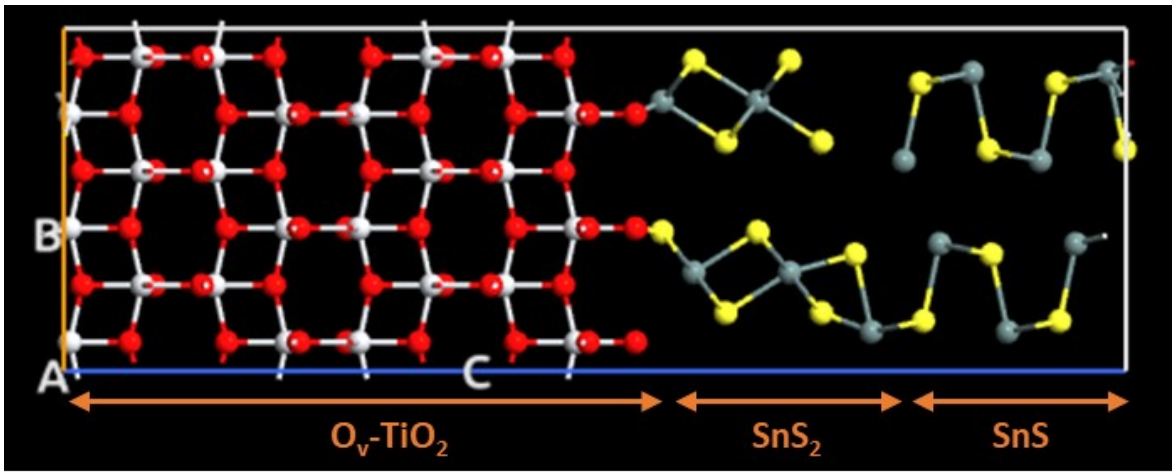

Fig. S14. The primary crystal structure of 3 main layers in the O_v-TiO_2-SnS/SnS_2 layers.

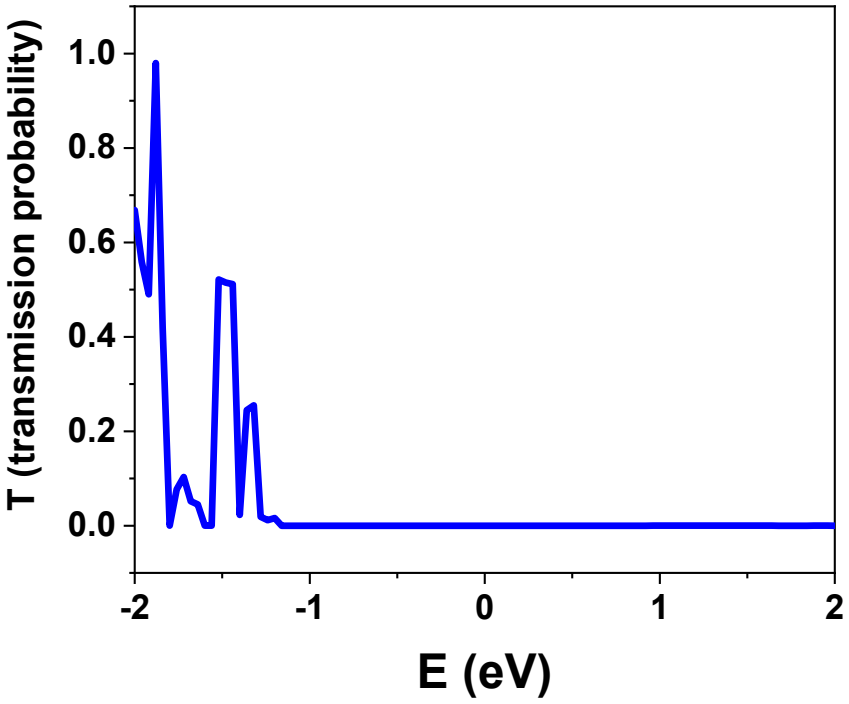

Fig. S15. Electron transmission spectrum through the O_v-TiO_2-SnS/SnS_2 system in respect of applied potential (light radiation).

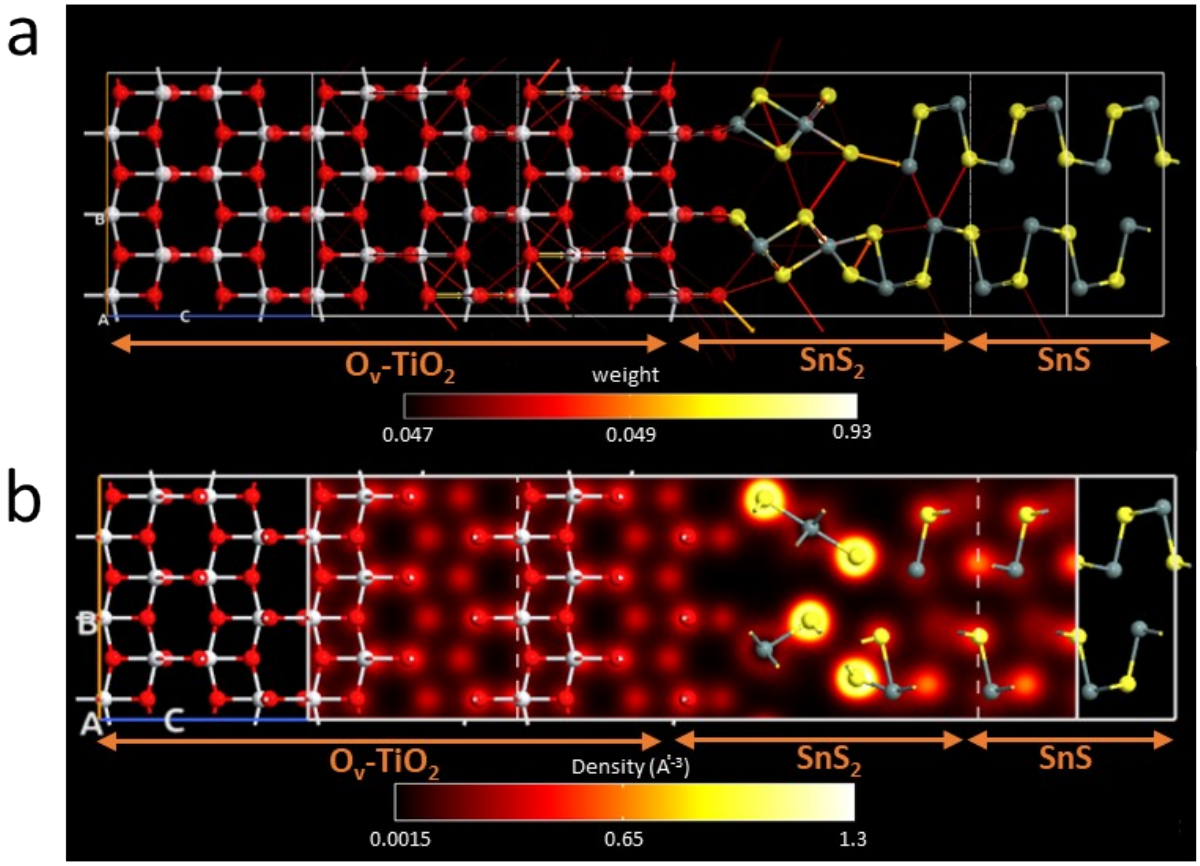

Fig. S16 (a) Transmission intensity of electrons passage, (b) Density of electrons passage through the photocatalyst layers of TiO_2-SnS/SnS_2.

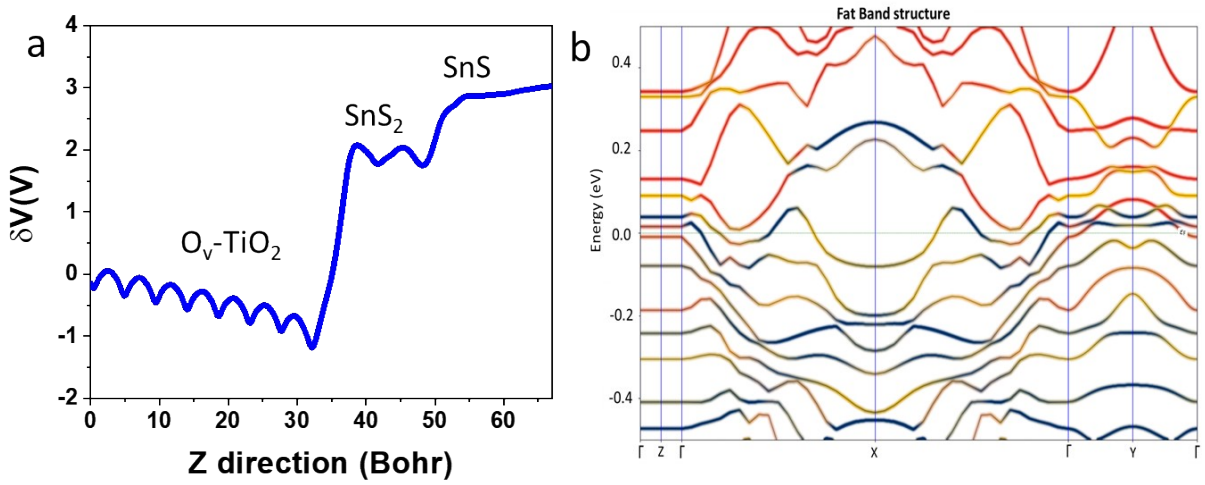

Fig. S17 (a) Potential vs. direction in TiO_2-SnS/SnS_2 (1 bohr = 0.52918 angstroms). (b) Fat band diagram of different atomic orbitals on the electronic properties around the Fermi level of TiO_2-SnS/SnS_2 (dominate role of P-orbitals of sulfur (orange curve) and d-orbitals of titanium (red curve).

Table S1. The presence of O and S-related energy states on fabricated Ti-based heterostructures estimated from the XPS analysis

Samples	**O 1s (at%)**			**S 1s (at%)**	
	O_L (%)	**O_V (%)**	**O_C (%)**	**Sn-S (%)**	**S^2 (%)**
TiO_2 NFs	80.45	4.39	15.17	--	--
TiO_2-SnO NFs	79.26	15.54	5.20	--	--
TiO_2-SnS (0.5:2) NFs	78.87	19.23	1.80	67.30	27.30
TiO_2-SnS/SnS_2 (2:2) NFs	28.65	60.63	10.72	84.36	13.61
TiO_2-SnS_2 (2:0.5) NFs	67.85	27.67	4.47	78.56	20.62

Table S2. Comparison of activity with reported photocatalytic nitrogen fixation.

Catalyst	Scavenger	Light source	Ammonia yield ($\mu mol.\ g^{-1}.\ h^{-1}$)	Ref
TiO_2-SnS/SnS_2	None	> 420 nm	517	This work
		Full spectrum	1179	This work
Au/TiO_2	20vol% Ethanol	300 W Xe-lamp	56.3	[1]
V_{Zn}/$Zn_3In_2S_6$	Methanol	$\lambda \geq 420$ nm	164.4	[2]
MoS_2/CdS	Methanol	300 W Xe-lamp	173.3	[3]
		$\lambda \geq 420$ nm		
$Mn_{0.5}Cd_{0.5}S$	Methanol	$\lambda \geq 420$ nm	121.9	[4]
/$CoTiO_3$	(10 vol%)			
Ru-TiO_2	None	Full spectrum	315	[5]
TiO_2/g-C_3N_4	None	$\lambda \geq 420$ nm	485	[6]
TiO_2-Au-BiOI	None	Full spectrum	543.5	[7]
BiOBr/TiO_2	None	Full spectrum	950	[8]
TiO_2/MIL-	20 vol% methanol	simulated sunlight	1084.31	[9]
88A(Fe)/g-C_3N_4				
TiO_2-Au-BiOI	None	UV-vis	534.5	[10]
AgCl/d-Bi_2O_3	None	Vis (400W Xe)	606	[11]
TiO_2 (OVs)	10 vol% methanol	Simulated sunlight	324.86	[12]
$CaTiO_3$ (OVs)	1 vol% methanol	Natural sunlight	236.12	[13]

Reference

[1] S. Liu, Y. Wang, S. Wang, M. You, S. Hong, T.-S. Wu, Y.-L. Soo, Z. Zhao, G. Jiang, Q. Jieshan, B. Wang, Z. Sun, Photocatalytic fixation of nitrogen to ammonia by single Ru atom decorated TiO_2 nanosheets, ***ACS Sustainable Chemistry & Engineering***, 7 (2019) 6813-6820.

[2] H. Han, Y. Yang, J. Liu, X. Zheng, X. Wang, S. Meng, S. Zhang, X. Fu, S. Chen, Effect of Zn vacancies in $Zn_3In_2S_6$ nanosheets on boosting photocatalytic N_2 fixation, ***ACS Applied Energy Materials***, 3 (2020) 11275-11284.

[3] X. Zheng, H. Han, J. Liu, Y. Yang, L. Pan, S. Zhang, S. Meng, S. Chen, Sulfur vacancy-mediated electron–hole separation at MoS_2/CdS heterojunctions for boosting photocatalytic N_2 reduction, ***ACS Applied Energy Materials***, 5 (2022) 4475-4485.

[4] H. Lv, M. Zhan, G. Li, F. Zhang, Z. Suo, C. Zhou, B. Wan, G. Wang, Y. Liu, Construction of a direct Z-scheme $Mn_{0.5}Cd_{0.5}S/CoTiO_3$ heterojunction with enhanced photocatalytic nitrogen fixation performance, ***Applied Surface Science***, 655 (2024), 159572.

[5] G. Ren, M. Shi, S. Liu, Z. Li, Z. Zhang, X. Meng, Molecular-level insight into photocatalytic reduction of N_2 over by electronic Metal-support interaction, ***Chem. Eng. J***. 454 (2023) 140158.

[6] S. Wu, C. He, L. Wang, J. Zhang, High-efficiency electron tandem flow mode on carbon nitride/titanium dioxide heterojunction for visible light nitrogen photo fixation, ***Chem. Eng. J***. 443 (2022) 136425.

[7] X. Yu, H. Qiu, Z. Wang, B. Wang, Q. Meng, S. Sun, Y. Tang, K. Zhao, Constructing the Z-scheme TiO_2/Au/BiOI nanocomposite for enhanced photocatalytic nitrogen fixation, ***Appl. Surf. Sci***. 556 (2021) 149785.

[8] X. Su, X. Zhang, M. Gao, X. Li, J. Chang, L. Hu, D. Geng, Y. Ren, T. Wei, J. Feng, Electron deficient $Bi^{3+\delta}$ serves as N_2 absorption sites and inhibits carriers recombination to enhance N_2 photo-fixation in BiOBr/TiO_2 S-scheme heterojunction, ***Journal of Colloid and Interface Science***, 663 (2024), 61-72.

[9] Q. Ding, X. Zou, J. Ke, Y. Dong, Y. Cui, H. Ma, Enhanced artificial nitrogen fixation efficiency induced by construction of ternary TiO_2/MIL-88A(Fe)/g-C_3N_4 Z-scheme heterojunction, ***Journal of Colloid and Interface Science***, 649 (2023), 148-158.

[10] X. Yu, H. Qiu, Z. Wang, B. Wang, Q. Meng, S. Sun, Y. Tang, K. Zhao, Constructing the Z-scheme TiO_2/Au/BiOI nanocomposite for enhanced photocatalytic nitrogen fixation, ***Applied Surface Science***, 556 (2021), 149785.

[11] X. Gao, Y. Shang, L. Liu, F. Fu, Chemisorption-enhanced Photocatalytic Nitrogen Fixation via 2D Ultrathin P-N Heterojunction AgCl/δ-Bi_2O_3 Nanosheets. ***Journal of Catalysis***, 37 (2019), 71-80.

[12] G. Zhang, X. Yang, C. He, P. Zhang, H. Mi, Constructing a tunable defect structure in TiO_2 for photocatalytic nitrogen fixation, ***J. Mater. Chem. A***, 8 (2020), 334- 341.

[13] A. Kumar, M. Kumar, V. N. Rao, M. V. Shankar, S. Bhattacharya, V. Krishnan, Unraveling the structural and morphological stability of oxygen vacancy engineered leaf-templated $CaTiO_3$ towards photocatalytic H_2 evolution and N_2 fixation reactions, ***J. Mater. Chem. A***, 9 (2021), 17006-17018.